# Cortical depth-dependent human fMRI of resting-state networks using EPIK

**Running title:** Whole-brain laminar fMRI in humans using EPIK

**Authors**

Patricia Pais-Roldán[1], Seong Dae Yun[1], Nicola Palomero-Gallagher[2-4], N. Jon Shah[1,5-7 *]

[1]Institute of Neuroscience and Medicine 4, Medical Imaging Physics, Forschungszentrum Jülich, Germany

[2]Institute of Neuroscience and Medicine 1, Structural and Functional Organisation of the Brain, Forschungszentrum Jülich, Germany

[3]C. & O. Vogt Institute for Brain Research, Heinrich-Heine-University, 40225 Düsseldorf, Germany

[4]Department of Psychiatry, Psychotherapy and Psychosomatics, Medical Faculty, RWTH Aachen, Aachen, Germany

[5]Institute of Neuroscience and Medicine 11, Molecular Neuroscience and Neuroimaging, JARA, Forschungszentrum Jülich, Germany

[6]JARA - BRAIN - Translational Medicine, Aachen, Germany

[7]Department of Neurology, RWTH Aachen University, Aachen, Germany

*** Corresponding author:**

Prof. N. Jon Shah

Institute of Neuroscience and Medicine 4, Medical Imaging Physics, Forschungszentrum Jülich, 52425 Jülich, Germany

Tel: +49 2461 61 6836, Fax: +49 2461 61 8294, Email: n.j.shah@fz-juelich.de

**Author Contributions**

N.J.S. designed the research; S.Y. developed the MR imaging sequence and the corresponding image reconstruction software; S.Y. and P.P. performed in vivo experiments. P.P. designed and performed data analysis; P.P. wrote the manuscript and prepared figures; N.J.S. invented the original EPIK sequence; N.P.-G. verified the anatomical labels and wrote the cytoarchitecture-related discussions; S.Y., N.P.-G. and N.J.S. reviewed the manuscript.

**ACKNOWLEDGEMENTS**

We thank Dr. Michael Schwerter for guidance in the phase-signal processing; Ms. Elke Bechholz and Ms. Anita Köth for technical support; Ms. Claire Rick for manuscript corrections; Prof. Zuo for guidance on the usage of CCS, and the fMRI volunteers for their excellent cooperation.

**ABSTRACT (190 words)**

Recent laminar-fMRI studies have provided substantial understanding of the *evoked* cortical responses in multiple sub-systems; in contrast, the laminar component of *resting-state networks* spread over the whole brain has been less studied due to technical limitations. Animal research strongly suggests that the supragranular layers of the cortex play a critical role in maintaining network communication; however, whether this is true in the human cerebral cortex remains unclear. Here, we used EPIK, which offers unprecedented coverage at sub-millimetre resolution, to investigate cortical broad resting-state dynamics with depth specificity in healthy volunteers. Our results suggest that human default mode network connectivity is primarily supported by intermediate and superficial layers of the cortex and that the preferred cortical depth used for communication can vary from one network to another. We also identified significantly lower ALFF and ReHo laminar slopes in scans acquired during task performance compared to rest, as well as varied laminar connectivity patterns. The evaluation of laminar-fMRI across the brain encompasses unprecedented computational challenges; nonetheless, it enables the investigation of a new dimension of the human neocortex, which may be key in the characterization of neurological disorders from a novel perspective.

**Keywords**

Cerebral cortex, Cortical Layer, Resting-state fMRI, High-resolution, EPIK

**Significance statement**

Resting-state networks sustain conscious awareness and diverse cognitive processing in the absence of tasks. In contrast to cortical *areas*, the cortical *depth* across different networks has been poorly investigated, mainly due to the small brain coverage enforced in high-resolution imaging methods. Here, using an optimized fMRI sequence, we demonstrate the critical involvement of the supragranular layers of the cerebral cortex in the maintenance of the resting-state dynamics. Given the cytoarchitectonics of the human neocortex, and based on our results, the cortical thickness constitutes an important dimension in the characterization of resting-state oscillations in the healthy brain, and its functional study may facilitate the identification of novel targets in neurological diseases.

**Key points:**

1. EPIK-fMRI of a motor task reproduces previous laminar activation profiles in M1.
2. Human resting-state network correlations peak at different cortical depths.
3. The cortical slope of ALFF and ReHo is decreased during task compared to rest.

## 1. INTRODUCTION

In the mammalian brain, the cerebral cortex is organized into specialized functional areas across its surface. In humans, the largest part of the cerebral cortex is occupied by the neocortex, where the perikarya of multiple neuronal cell types are organized into six horizontal layers. The layered structure of the neocortex, which can be characterized by its cytoarchitecture, is involved in specialized signal processing [1-3]. The functional specificity of the cortex at its different depths has been demonstrated in animals using multi-site electrodes and, more recently, with cell-specific calcium imaging, e.g., via two-photon microscopy or optical fibers [4-8]. Although electrophysiology can theoretically be performed in the human brain to investigate layer-specific activations, it is an extremely invasive technique, and, consequently, data are only available from select patient groups, e.g., in epileptic patients, who benefit from such an undertaking [9]. Moreover, although electrode recordings can provide direct information concerning layer activity, the coverage of electrophysiological recordings is limited by the number of multi-site electrodes, which is usually a single point at different depths. In contrast to the limitations of electrophysiology, functional magnetic resonance imaging (fMRI) can afford broad brain coverage non-invasively, although it is usually limited by relatively low temporal and spatial resolution. In rodents, experiments merging fMRI and axonal tracing maps demonstrated that layers 2/3, but not other cortical depths, project exclusively to areas within the default mode network [10], and it has been shown that stimulation of upper, but not lower, sections of the motor cortex results in network-wide effects [11], suggesting a primary role of the superficial cortical laminae in resting-state networking. Due to a lack of non-invasive methods to sufficiently sample the cerebral cortex, the specific way in which the cortical neurons communicate with each other in the human brain -across different depths and through different areas- largely remains an open challenge, which could be addressed with novel high-resolution fMRI methods.

fMRI most commonly relies on the identification of blood changes, which, assuming perfect neuro-vascular coupling, represent neuronal function in the brain [12-14]. Despite its dependence on the vascular architecture of the cortex, laminar fMRI, i.e., sub-millimeter resolution fMRI acquired with the purpose of studying depth-specific neuronal responses, has proven to be a valuable tool for studying cortical dynamics in animals and humans [15-25]. Two main fMRI contrasts are usually employed in human laminar fMRI: cerebral blood volume (CBV), typically applied as part of vascular occupancy schemes (VASO), and blood oxygenation level dependent (BOLD). Although VASO offers high spatial specificity by detecting dilation of the microvasculature based on T1 contrast, it exhibits low sensitivity due to unwanted tissue suppression by an inversion recovery pulse [26-28]. In contrast, sequences based on BOLD present the advantage of a higher signal-to-noise ratio (SNR), with spin-echo-based (SE) echo planar imaging sequences (EPI) offering greater parenchymal specificity and gradient-echo (GE) schemes offering the best sensitivity [27]. The higher SNR and the flexibility of being able to accommodate higher sampling rates make GE sequences some of the most commonly used in the fMRI field, typically in the form of GE-EPI. Due to GE schemes having enhanced sensitivity to large vessels [29], e.g., pial veins, with long T2* constants, several methods have been presented for use in the pre-processing pipeline to ameliorate contamination from extra-parenchymal signals or to correct the evoked activation profile across cortical depths [30-36].

fMRI acquired with different contrasts and sub-millimeter resolution has enabled the function of the cerebral cortex to be sampled with column- and layer-specificity in the context of sensory, motor, visual and auditory tasks [15, 17-25, 37-39] and has shown the superficial layers of the neocortex to be predominantly involved in the processing of neuronal signals. This predominance is possibly due to the fact that layer III is the main source and target of cortico-cortical connectivity [40], and that the higher synaptic density found there compared to the remaining cortical layers is associated with higher receptor densities [1]. Importantly, a study focusing on the visual cortex reported correlations between the function of specific layers imaged with fMRI and particular EEG rhythms [41], reinforcing the potential for using fMRI to detect layer variability.

In contrast to task-related circuits, which are usually limited to specialized responses in a small portion of the cerebral cortex, during rest, cross-talk between distant cortical areas maintains a baseline neurological state [42]. Although the potential for using fMRI to sample cortical layers is clear, the limited brain coverage enforced by most existing high-resolution-fMRI schemes precludes the investigation of large-scale inter-regional depth-dependent connections; i.e., some resting-state evaluations have been presented previously, but these mostly focused on particular systems, e.g. [18, 43]. To date, only a few groups have reported fMRI acquisitions from the whole brain at ≤ 1 mm resolution [44-46], and, to our knowledge, only one study has intended to use laminar fMRI to uncover the cross-layer functional interactions that exist in the human brain during rest with a nominal spatial resolution of $0.8 \times 0.8 \times 0.8$ mm$^3$ [46].

Here, we applied TR-external EPI with keyhole (EPIK) to identify the laminar signals from most of the cerebral cortex with a 0.63 mm iso-voxel size in healthy volunteers. It has been previously shown that EPIK [47-52] can offer higher spatial resolution in dynamic MR studies with comparable hemodynamic-response detection compared to routine EPI [53-57]. Moreover, the combination of TR-external phase correction with EPIK has been shown to further enhance spatial resolution [58]. In this work, TR-external EPIK covered the human cerebrum almost entirely, with 123 slices sampling voxel volumes of ~ 0.25 mm$^3$. The combination of a smaller voxel size and near whole-brain coverage is a key feature of this work when compared to previous laminar fMRI studies. By adding pre-processing steps to ameliorate the potential bias of the GE sequence, the acquired images allowed us to perform cortical depth-dependent analysis of broad resting-state networking in the human brain.

## 2. MATERIALS AND METHODS

### 2.1. Subjects:

The functional data from thirteen healthy volunteers (eleven males and two females; age, 23-47 years; 12/13 right-handed, 1/13 left-handed [59]) were included in this study. Although eighteen subjects were originally measured, four of them were removed from the study due to the lack of/non-proper physiological recordings, and an additional set of data was removed after detecting high levels of motion. Hence, the structural scans of eighteen subjects were used for the anatomical study of the cortex, but only data from thirteen subjects were included in the functional analysis relevant to the majority of the results shown in this manuscript. Subjects were scanned in one single session for a period of ~55 min, which included two resting-state fMRI scans ('rs-fMRI-1' and 'rs-fMRI-2'), one finger motor task fMRI scan ('task-fMRI'), and an MP2RAGE scan. Due to poor anatomical-functional co-registration, the rs-fMRI-2 data from one subject were omitted, and another subject was excluded from both the rs-fMRI-2 analysis and the whole-brain laminar evaluations of the task-fMRI for the same reason (i.e., the number of subjects used in the whole-brain analysis were 13, 11 and 12 for rs-fMRI-1, rs-fMRI-2 and task-fMRI, respectively). However, the task-fMRI data from all 13 subjects were used for the analysis of evoked responses in the primary motor cortex (M1) as the motor cortex could be well co-registered in all subjects. A pneumatic belt was positioned around the subject's chest, and a pulse oximeter was placed on the 2$^{nd}$, 3$^{rd}$, or 4$^{th}$ finger of the left hand to control for potential interference of the physiological signals on the fMRI responses [60]. The experimental methods were approved by the local institutional review board (EK 346/17, RWTH Aachen University, Germany), MR-safety screening was performed prior to MRI acquisition, and informed written consent was obtained from all subjects.

### 2.2. Experimental design:

In the rs-fMRI, subjects were asked to remain still, awake, with eyes closed, and without thinking about anything in particular. In total, 172 volumes were reconstructed from the rs-fMRI (~10 min). For task-fMRI, subjects were asked to follow instructions on a projected screen and to perform flexion of the right index finger without necessarily touching the thumb. The task was performed continuously at a comfortable pace (1-2 Hz, for most subjects) for 21 s and was repeated 12 times, alternated with 21 s of rest. In total, 148 volumes were obtained (4 s rest, [21 s task, 21 s rest] × 12) (~ 8.6 min). One subject was invited to participate in an additional scan session and first performed a finger motor task (4 s rest, [21 s task, 21 s rest] × 8), followed by a finger motor and sensory task, i.e., instructions were given to approach the right index finger towards the thumb involving touching (4 s rest, [21 s task, 21 s rest] × 8).

### 2.3. MRI data acquisition:

MRI data were collected on a Siemens Magnetom Terra 7T scanner with a 1-channel Tx / 32-channel Rx Nova Medical head coil. An anatomical MRI volume was acquired using an MP2RAGE sequence, TR/TE = 4300/2 ms, matrix = 256 × 376 × 400 (0.60 × 0.60 × 0.60 mm$^3$). Functional MRI data were obtained using GE-EPIK combined with a TR-external EPI phase correction scheme. The sequence performance has been previously

described elsewhere and briefly consists of a full sampling of central k-space (48 central lines) and a sparse sampling of the peripheral k-space (288 lines), which is completely acquired after three TRs, i.e., every TR encompasses the acquisition of the k-space center and 1/3 of the periphery (details of the sequence can be found in previous publications [52-54, 57, 58]). Sampling the central k-space at every TR ensures a near optimum SNR for each individual scan. An analysis of raw data from a healthy subject in our preliminary study showed that the central k-space in the current configuration has 86.5% of the entire k-space energy, whereas including the peripheral k-space lines that are continuously updated at every scan (i.e. 1/3 of the periphery) results in 91.0% of the entire energy. Two acquisition protocols were used to collect data in this study. In both protocols, TR/TE = 3500/22 ms, FA = 85°, partial Fourier = 5/8, 3-fold in-plane/3-fold inter-plane (multi-band) acceleration, bandwidth = 875 Hz/Px and αPC/αMain = 9°/90°. B0 shimming was performed with a standard routine provided by the manufacturer. For protocol-1 (used to generate all the data in the main figures), matrix = 336 × 336 × 123 slices (0.63 × 0.63 × 0.63 $mm^3$). For protocol-2, matrix = 408 × 408 × 105 slices (0.51 × 0.51 × 1.00 $mm^3$). The main figures show results acquired with protocol-1 (i.e., isotropic voxels).

### 2.4. Data analysis:

A summarized pipeline of our pre-processing methods can be found in **Figure 1**. Briefly, cortical surfaces were extracted from the anatomical scan and used as a template to map the functional signals using Freesurfer (Martinos Center for Biomedical Imaging, Charlestown, MA). The assessment of the cortical model (results in **Fig. S1**) is based on the excellent work by Kay et al. [29]. Pre-processing was mainly done on AFNI (Analysis of Functional NeuroImages, NIH, Bethesda, MD), and included correction of the magnitude time course to minimize large-vein contribution (**Fig. 2**), as previously described [30, 31, 61], in conjunction with common pre-processing steps (slice-timing correction, realignment, temporal filtering and regression of motion parameters and averaged white matter and CSF time courses), which resulted in zero-mean "clean" functional time courses (**Fig. 1**). For the assessment of the resting-state measures in task-related scans, the task predictor time course was added as a regressor-of-no-interest so as to avoid interference from an active motor pathway on the assessed metrics (for comparison, the power spectrum and connectivity measures were assessed in all conditions, including the task scan with and without regression of the task paradigm). Post-processing analysis included volume-based ICA-analysis, surface-based temporal correlation (i.e., functional connectivity), surface-based spectral decomposition, amplitude of low-frequency fluctuations (ALFF), surface-based regional homogeneity (ReHo) and, in task fMRI only, surface-based general linear model (GLM) analysis. Post-processing was performed using 3dRSFC on AFNI, Matlab scripts (Mathworks, Natick, MA) and melodic on FSL (FMRIB Software Library, Oxford, UK). The implementation of surface ReHo was based on the functions of the Connectome Computation System ([62]). Volume-based analyses (ALFF and ICA) were followed by a volume-to-surface projection and averaging of vertices within each ROI for a total of 42 ROIs (21 per hemisphere, see **Table 1**) and each surface. Normalization of functional connectivity, ALFF, and ReHo was performed by subtracting the mean value across the brain and dividing by the standard deviation. Computations involving sulcal or gyral locations were restricted to vertices corresponding to the top or bottom 20% curvature values, respectively.

Note that the term "surfaces" or "layers" employed through the manuscript should not be interpreted as histologically-defined cortical layers; instead, the terms are employed to refer to each of the six different cortical depths that are artificially generated by splitting the cortical thickness into five different compartments. A more detailed explanation of the methods used to generate the presented results can be found in the *Supplementary Material*.

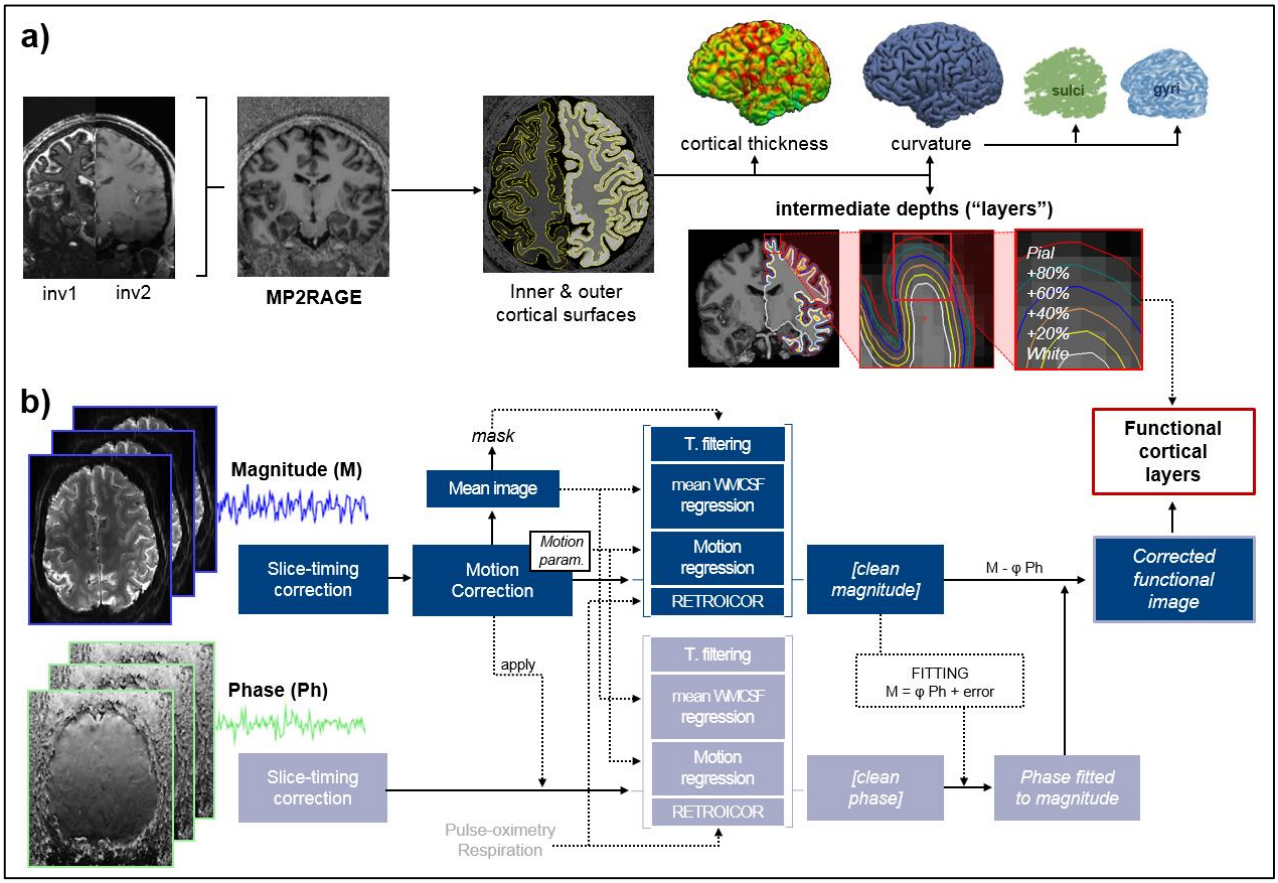


***Figure 1. Main steps for pre-processing of the anatomical (a) and functional scans (b). a)*** *"inv1" and "inv2" indicate the first and second inversion contrast images of MP2RAGE. The T1-weighted MP2RAGE is used to segment the brain into gray matter, white matter, and cerebrospinal fluid (CSF). The cerebral cortex (outer brain gray matter) is further processed to extract its boundaries (outer or "pial" and inner or "white"). Several calculations can be performed based on these surfaces (e.g., thickness, curvature). Four additional surfaces are generated at equal spacing.* ***b)*** *Both the magnitude and phase images obtained with TR-external EPIK are subjected to a routine pre-processing pipeline, including slice timing correction, motion correction, regression of physiological signals, and temporal filtering. The pre-processed phase image is used to correct the magnitude image from vein-related bias. The corrected pre-processed magnitude functional image is then projected onto the six generated surfaces, in subject space, for laminar fMRI analysis.*

## 3. RESULTS

### 3.1. Characterization of the cortical template for whole-brain laminar mapping

In a recent report, we have demonstrated the feasibility of using TR-external EPIK to assess fMRI activity over a large FOV with submillimeter spatial resolution [51]. The additional acquisition of a structural MP2RAGE sequence enabled us to produce a surface model of the cerebral cortex for each subject. Based on this model, it was possible to study brain activity at six different cortical depths, referred to hereafter as "layers" (different from the cytoarchitectonically-defined cortical layers) and specified as "pial, +80%, +60%, +40% +20%, and white", from the most superficial to the deepest portion of the cortex, respectively. These layers were used as a template for analysis of the functional data (see *Methods* and **Fig. 1**). **Figure S1** provides a characterization of the cortical model. In **Figure S1a**, an example of the distribution of sulci and gyri, i.e., the curvature of the cerebral cortex and cortical thickness, is provided for a representative coronal slice. The spatial resolution of each surface was assessed in sulci and gyri independently. As the cortical surfaces were generated by inflating the inner cortical boundary towards the pial space, a one-to-one correspondence between vertices existed across all surfaces; hence, the in-surface resolution varied depending on the depth and the curvature (for a visual example, see insets in **Fig. S1b**). The histograms in **Figure S1b** show the distribution of vertex-to-vertex distances at different cortical depths for gyri (blue) and sulci (green), in both cerebral hemispheres, as a mean ± standard deviation (SD), obtained from an 18-subject group. In agreement with previous work [29], it was observed that, in gyri, the vertex-to-vertex distance increased from 'white' to 'pial'; on average, a sparse distance of 0.72±0.04 mm existed between the vertices in the pial surface, whereas this distance was 0.49±0.01 mm in the white surface, i.e., the surface spatial resolution improved with depth in gyri locations. In contrast, in sulci, the vertex-to-vertex distance decreased from 'white' to 'pial', with an average of 0.36±0.01 mm between consecutive vertices in the pial surface vs. 0.49±0.02 mm between the vertices of the deepest layer, i.e., outer surfaces were more densely sampled in sulci. This feature was observed in both the left and right hemispheres. The upper inset in **Figure S1b** exemplifies the larger vertex-to-vertex distance in the superficial layers of the cortical gyri, and the inset below exemplifies the larger distance between consecutive vertices in gyri compared to sulci. Cortical thickness was calculated in both cerebral hemispheres for 21 ROIs and for gyri and sulci in the whole cortex (**Fig. S1c**). Note that the analysis specific to gyri or sulci only considered the bottom 20% and top 20% curvature values, respectively (see *Methods*). Given that the cortical ribbon is thicker in the crown of gyri than in their walls or in the fundus of sulci [29] (**Fig. S1c**, blue bar vs. green bar), the layer-to-layer separation is greater at this position of the gyri (**Fig. S1d**, 0.62±0.02 mm between layers of cortical gyri vs. 0.40±0.01 mm in sulcal locations), which indicates that higher signal contamination from neighboring layers can be expected in sulci, particularly in their fundus. Note that the in-depth resolution in the crown of gyri, i.e., the inter-layer distance, approximately corresponds to the voxel size employed in our fMRI protocol. The relative differences in surface resolution and inter-layer distance across cortical depths are in broad agreement with the study of Kay et al. [29]. However, their results showed a slightly better surface resolution, which was probably due to having increased the density of surface vertices during processing, a step that was avoided here to limit the computational demands of the whole-cortex functional analysis. The

characterization of the cortical surfaces suggested that the chosen subject-specific cortical model could be used as a reliable template to map functional signals and to study layer-based functional oscillations.

### 3.2. **De-veining of the high-resolution GE-EPIK**

Given the susceptibility of GE images to the signal of ascending venules and pial veins, we adopted the correction method described by Menon et al. [30, 31]. This method consists of using the information in the phase signal, which is presumably proportional to changes in oxygenated/deoxygenated hemoglobin in non-randomly oriented vessels, to remove unwanted signal change from the magnitude signal. The procedure should, therefore, minimize the contribution of large vessels (mainly in upper cortical layers and veins in the CSF compartment) while preserving the signal of the gray matter capillaries. **Figure 2** exemplifies the correction method by displaying the magnitude, phase, and corrected magnitude signal time course in four voxels located at different cortical depths in the precentral gyrus during task performance (the same method was applied to the resting-state data). The signal of a voxel near the CSF ("1" in **Fig. 2c**) is substantially affected by Menon's de-vein procedure, but the change is much less evident in deeper gray matter voxels (e.g. "4" in **Fig. 2c**). The contribution of large vessels can be minimized by using this correction step, allowing certain cortical-depth functional signatures to be detected, as shown in the following paragraphs.

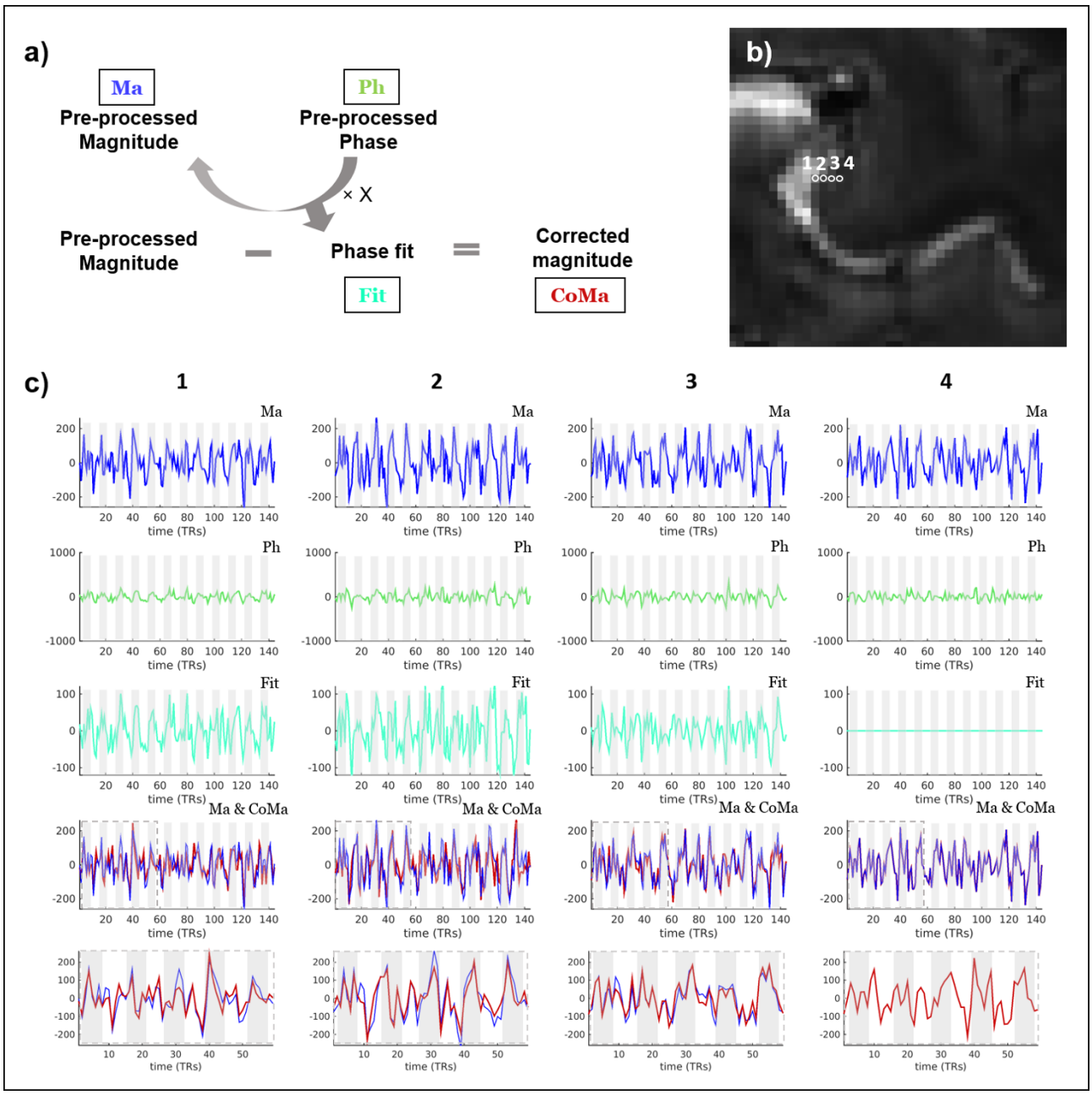


***Figure 2. Phase-based de-vein procedure. a)*** *Summarized procedure for voxel-wise de-veining based on phase information.* ***b)*** *Location of voxels selected to investigate the effect of the correction procedure, depicted with white circles (1 to 4). "1" corresponds to a voxel next to CSF and "4" to deep gray matter.* ***c)*** *fMRI signal time course at different points in the correction procedure for the four voxels examined during a motor task. Shaded bars within each plot represent time periods corresponding to finger-tapping. The time-varying signal magnitude (top panels, in blue) is corrected by subtracting a weighted version of the phase (phase fit, in cyan). The two bottom rows show the corrected time course (in red) as well as the original magnitude time course (blue line) for comparison. The last row in panel c depicts the same time courses as in the fourth row but only until the 60$^{th}$ TR to aid visual inspection. Note the relatively big effect of the procedure on the surface of the brain (bottom left panel in c) compared to deeper regions (bottom right panel in c) that are less contaminated by ascending venules and large vein bias.*

### 3.3. Depth-dependent evoked responses in the primary motor cortex (M1)

In order to prove the capabilities of TR-external EPIK for use in a laminar analysis of the whole brain, we first aimed to reproduce the results obtained in previous fMRI studies of finger-motor tasks. These results are characterized by a strong response in the upper layers of M1 and a second activation peak in the middle-deep layers when avoiding non-corrected GE-BOLD sequences [18-20]. A task-based fMRI protocol consisting of 12 epochs, alternating 21 s blocks of finger motion with 21 s blocks of rest, was conducted on each subject using a submillimeter-resolution protocol configured with TR-external EPIK; voxel size: 0.63 mm isotropic, matrix: 336 × 336, 123 slices (see protocol-1 in *Methods*). In agreement with the previous literature [18-20], we observed a marked predominance of the BOLD response in the superficial layers of M1 (**Fig. 3**). A monotonous signal decrease from superficial to deep layers, typical in laminar GE-BOLD, was observed after averaging the beta coefficient within a portion of M1 (**Fig. 3a-c**, N=13), possibly reflecting a bias due to ascending veins and large venous vessels located on the surface (**Fig. S2**) that may remain even after the de-veining procedure. However, when sampling the beta-map of area M1-4A [63] (specifically, along 20 lines, each extending from the CSF and up to the WM), we were able to identify a bimodal response superimposed over this gradient in multiple subjects and through several consecutive slices (see mean line profile in **Fig. 3d** and several examples through **Fig. 3j-m**). This laminar activation profile was approximated significantly better by polynomials of degree > 2 compared to a linear fitting (**Fig. S3**) and resembled the typical profile of finger motor tasks finely assessed in high-resolution schemes [18-20]. The specificity of laminar responses was further evaluated in one subject by comparing the activation profiles of two different tasks: movement-only, or movement + touch, i.e., somatomotion, or movement + somatosensation (**Fig. 3m**). While both tasks resulted in an initial activation peak in the superficial layers, the relatively salient response observed in deeper layers during movement was minimized and shifted towards more superficial layers upon the addition of touch. It is worth noting that the post-hoc correction steps to ameliorate the GE-BOLD signal bias towards pial vessels did not include deconvolution of model signal bias across the cortical ribbon (in order to keep consistent pre-processing across task and resting-state data). Although data are likely to be partially biased towards the surface, these results demonstrate the potential of TR-external EPIK to track laminar changes in the human cortex, even without the application of deconvolution procedures.

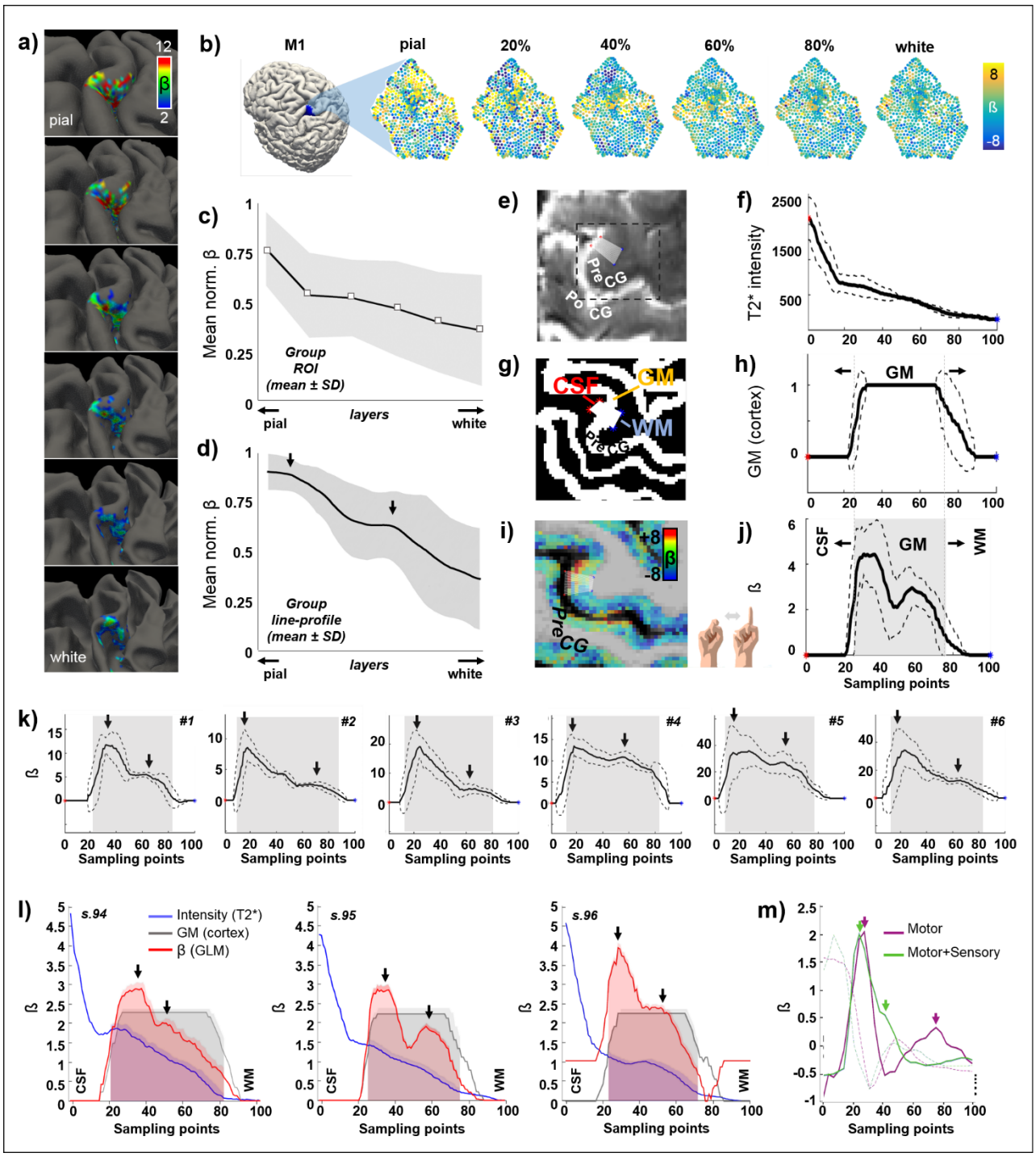


***Figure 3. Cortical depth-dependent motor task-evoked BOLD fMRI. a)*** *Six panels showing the surface beta-map of a selected ROI over different cortical depths of M1, resulting from a finger motor task in a representative subject.* ***b)*** *Flattened patches of the ROI in M1 extracted from six surfaces at different cortical depths.* ***c)*** *The plot shows the mean ±SD of the normalized beta-coefficient along six different cortical depths, from the pial surface of the brain towards the inner white matter boundary (N=13).* ***d)*** *Mean ±SD of the activation line-profiles, computed from the beta map of 13 subjects, using a line-profile method on a particular segment of M1 (computation explained through panels e)-j)).* ***e)*** *The figure shows part of a mean TR-external EPIK axial slice containing the precentral gyrus (PreCG). The twenty overlaid sampling lines (in white) extend from the cerebrospinal fluid (CSF), covering the cortical thickness, up to the white matter (WM).* ***f)*** *Average*

*line profile of the mean TR-external EPIK on the selected sampling region (the 20 lines on e)). Note the high intensity at the initial points (CSF, with long T2 constant). The discontinued lines above and below the solid line represent the mean ±SD.* ***g)*** *Same region as in e), cropped from the segmented MP2RAGE, which identifies the cortical ribbon (in white color, labeled as gray matter (GM)).* ***h)*** *Line profile calculated from the sampling lines over the image in g).* ***i)*** *Beta coefficient map overlaid on the MP2RAGE.* ***j)*** *Profile of the beta coefficient along the selected lines crossing the finger area in the PreCG. Note the higher signal on superficial and middle layers of the cerebral cortex (double peak, typical of motor tasks). The gray-shaded area in j) represents the extent of the gray matter, with superficial layers (i.e., pial surface) on the left, near the CSF, and deep layers (i.e., white surface), on the right, near the white matter.* ***k)*** *Six subject-specific examples of line-profiles corresponding to a right finger motor task. The black arrows highlight the most salient signals across the cortical ribbon.* ***l)*** *Three examples showing the line profiles of the beta map in three consecutive slices (s94.s96) for one particular subject.* ***m)*** *Line profiles in a different subject performing either a finger movement only (purple trace) or a finger movement involving touch (green trace). Dashed lines indicate the intensity of the mean functional image for each task-fMRI scan for spatial reference. PoCG post-central gyrus.*

### 3.4. Near whole-brain assessment of cortical depth-dependent activity in resting-state fMRI

To investigate whole-brain depth-dependent functional measures and cross-layer interactions between distant cortical areas during rest, we acquired two additional task-negative fMRI scans from each subject, one using protocol-1, with 0.63 mm isotropic voxels, i.e., same as for the task-fMRI, and another using protocol-2, with higher in-plane resolution (0.51 × 0.51 $mm^2$) and thicker slices (1.00 mm) to maintain a reasonable SNR level. In order to reduce the dimensionality of our data (6 surfaces × ~ 290 000 vertices per hemisphere), we first segmented the cerebral cortex into 21 ROIs related to well-known brain networks: default mode, visual, sensory-motor, auditory, executive control, and salience (**Table 1**). Having averaged the vertices within each ROI and each cortical layer in both cerebral hemispheres, we obtained 252 time courses from each fMRI scan (21 ROIs × six surfaces × two hemispheres). These were then subjected to several analysis methods. Following a frequency-power decomposition of the functional time courses, it was found that most cortical areas exhibit a higher level of activity in their superficial layers (**Fig. 4a**). This activity was observed to oscillate mostly within the range 0.01-0.03 Hz, which is in agreement with other non-laminar rs-fMRI studies focusing on cortical gray matter [64-67]. Integration of the signals fluctuating between 0.01 and 0.1 Hz, i.e., the typical range considered in rs-fMRI studies [68], provided a simplified measure of brain activity during rest, commonly denoted as ALFF, which was assessed for each ROI and the six different cortical depths. The two panels in **Figure 4b** show the dependence of resting-state activity on cortical depth for each cerebral hemisphere, sorted by networks (in different colors, according to **Fig. 4c**) and differentiated into whole-ROIs, sulci or gyri, of each ROI. To simplify the laminar profile, a linear fitting was calculated for each ROI, and the slope of the fitting line was computed per ROI (**Fig. 4d**) and per network (**Fig. 4e**). The level of activity was observed to decrease from the surface of the cortex towards the deep gray matter in most ROIs (negative slope), irrespective of whether these were assessed in cortical gyri or cortical sulci (**Fig. 4f**). Gyri and sulci showed significantly different ALFF slopes ($p<0.005$) in the anterior midcingulate cortex (hub in the salience network),

with gyri showing a steeper ALFF profile (green marker in **Fig. 4e**, middle vs. right panels); however, most of this ROI lies within the crown of a gyrus, and hence the results may be biased by a low number of vertices considered in sulcal locations. The auditory network seemed to have steeper ALFF profiles in sulci; however, the difference with respect to gyri was not significant (see purple marker in the same figure panels). The sensory-motor network and the auditory network exhibited the most and the least steep ALFF laminar profiles, respectively (**Fig. 4e**).

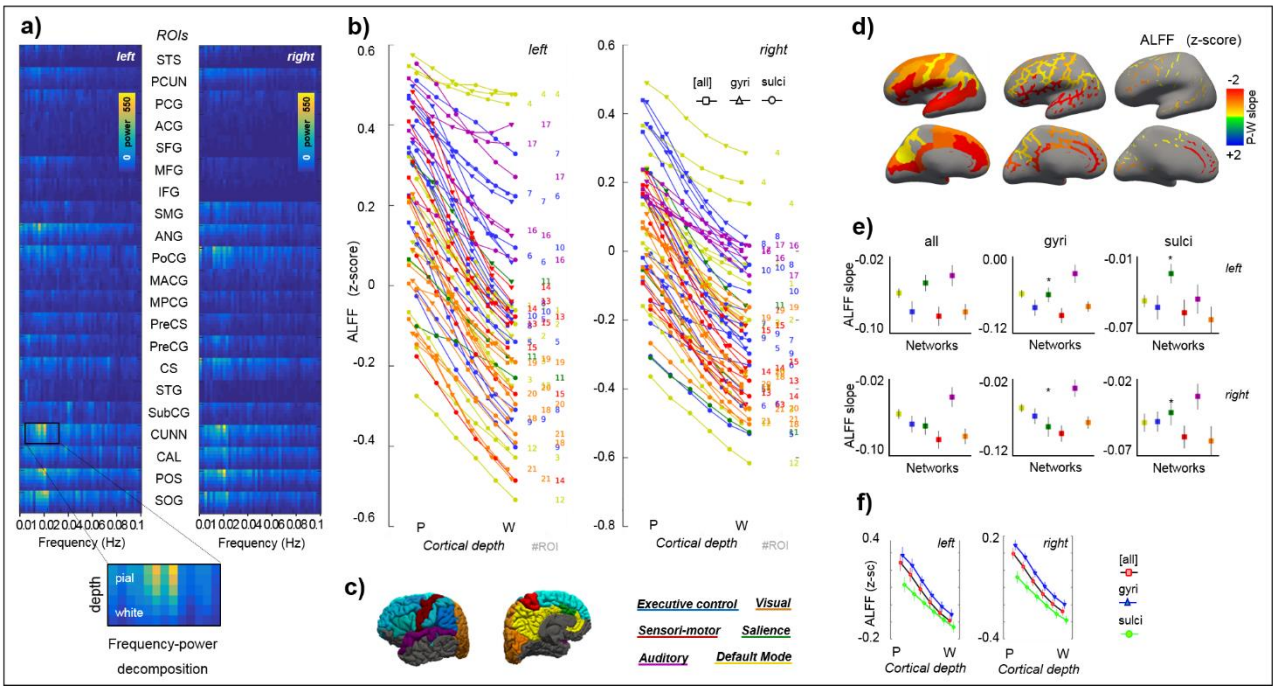


***Figure 4. Cortical depth-dependent resting-state activity. a)*** *Mean layer-specific frequency-power decomposition of the BOLD signal in 21 ROIs (both cerebral hemispheres), averaged across 13 subjects.* ***b)*** *The plots show the cortical depth dependence of the resting-state activity, measured as average ALFF, through all ROIs and both cerebral hemispheres. Numbers on the right of each line help to trace back each ROI (1 and 21 correspond to the first and the last ROI presented in a) –STS and SOG, respectively-). The line color indicates the network to which the ROIs are associated (see panel c). The squared, triangular or rounded symbols indicate whether the ROI was considered in its entirety, whether only the vertices corresponding to the most salient gyri in each ROI were considered, or whether only the vertices corresponding to the most salient sulcal locations in each ROI were considered, respectively.* ***c)*** *The figure displays the regions that were included in the functional analysis, organized by network, over the surface of the brain (see* ***Table 1*** *for a detailed description of the ROIs included).* ***d)*** *Brain surface maps showing the average slope of the fitting line that best approaches the depth-varying ALFF per ROI, per ROI gyri, and per ROI sulci.* ***e)*** *ALFF slope for each cortical network.* ***f)*** *Average ALFF per layer for whole ROIs, sulci, or gyri.*

The assessment of layer-specific regional homogeneity (ReHo) demonstrated curvature specific differences regarding the slope of this measure across the cortical thickness; while the ReHo slope was nearly flat or positive for most gyral locations, most ROIs exhibited a higher ReHo in the superficial layers of cortical sulci (e.g., negative slope in a pial→white direction, **Fig. 5a,** sulci, represented by ● vs. gyri, represented by ▲, **Fig.**

**5b** and **Fig. 5c**, middle vs. right panels). **Fig. 5d** shows the ReHo map (mapped from surface to volume space) for a representative subject. The ReHo slope in sulci was significantly different from that in gyri across all networks assessed ($p<0.05$,). It is worth considering that, although large veins are more likely to traverse the outer portion of the brain (i.e., gyral locations), the presence of small venules over the sulcal surfaces could contaminate a larger number of nearby brain vertices, yielding higher homogeneity measures among sulcal vertices. Whole-brain results are summarized in **Fig. 5e**.

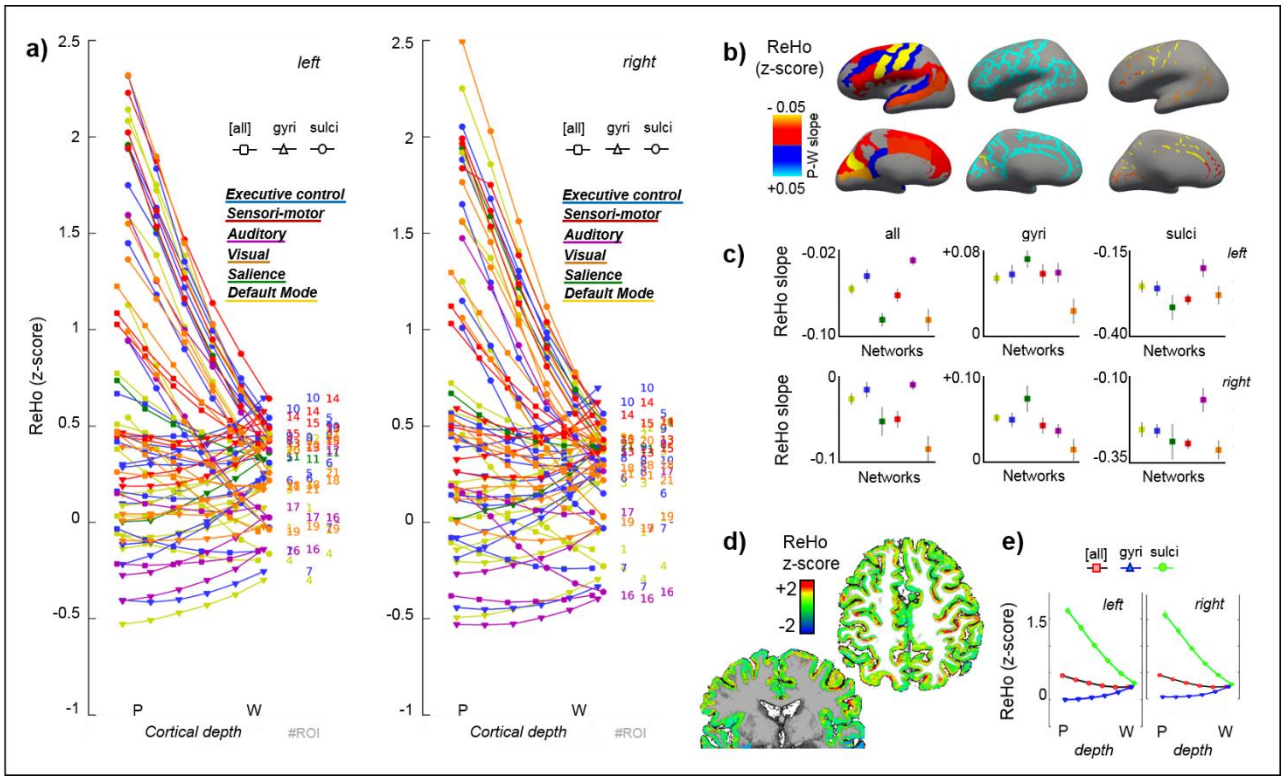


***Figure 5. Surface-based ReHo. a)*** *The plots show the cortical depth dependence of ReHo, computed within each surface, through all ROIs and both cerebral hemispheres. Numbers on the right of each line help to trace back each ROI (1 and 21 correspond to the first and the last ROI presented in Fig. 4a). The line color indicates the network to which the ROIs are associated (see Fig. 4c), and the squared, triangular or rounded symbols indicate whether the ROI was considered in its entirety, whether only the vertices corresponding to the most salient gyri in each ROI were considered, or whether only the vertices corresponding to the most salient sulcal locations in each ROI were considered, respectively.* ***b)*** *Brain surface maps showing the average ReHo slope of the fitting line that best approaches the depth-varying ReHo per ROI, per ROI gyri, and per ROI sulci.* ***c)*** *ReHo slope for each cortical network.* ***d)*** *Representative ReHo map projected from six cortical surfaces to volume space. Note the higher ReHo near the pial surface in sulci.* ***e)*** *Average ReHo per layer for whole ROIs, sulci, or gyri.*

In addition to using ALFF and ReHo to assess brain activity during rest, we investigated the connections between different brain regions at different depths of the cerebral cortex. This was done by generating a functional connectivity matrix from each fMRI scan, which included the temporal correlation between all pairs

of time courses, i.e., between the average time course of each region at each layer and that of every other region and layer (i.e., $252^2$ cells). The correlation values of the six layers in each ROI and the six layers of every other ROI were computed. For group analysis, the connectivity matrices of 13 subjects were averaged and subjected to a t-test for statistical thresholding. The resulting adjacency matrix was then used to generate a layer-specific, whole-brain connectivity graph. A whole-brain connectivity map was computed for each of the three scans acquired per subject, and the results are shown in **Figure S4i-l**. To facilitate the visual inspection of the depth-dependent connectivity graphs, the six assessed layers were grouped into "deep," "intermediate," and "superficial" layers, and connections were color-coded based on the pair of cortical depths involved, e.g., deep–deep connections were represented by yellow lines, intermediate–intermediate connections by red lines, deep-intermediate connections by orange lines, etc. In order to simplify the connectivity results, inter-regional connections were grouped per network. **Figure 6a-c** shows three versions of four network connectivity graphs, with variable layer visibility, demonstrating the depth-specific significant connections within the default mode network, the executive control network, the sensory-motor network, and the visual network, obtained from a resting-state scan acquired with protocol-1 (N=13). The same graphs were also computed from the task-based fMRI obtained with protocol-1 and the rs-fMRI obtained with protocol-2, which can be found in **Figure S5**. In most cases, connections involving deep layers of the cortex were reduced compared to more superficial ones (**Fig. 6c**, compared to 6a or 6b). A connectivity analysis based on coherence instead of temporal correlation rendered similar results (**Fig. S6**). The assessment of the cortical depth-dependent connectivity for each functional network, i.e., the average temporal correlation between ROIs of the network at each cortical depth, indicates that the superficial and upper-intermediate layers govern most resting-state correlations within the default mode network and the visual network (bell shapes with a peak on the left in **Fig. 6e**). The intermediate layers are seen to be strongly connected within the sensory-motor network (symmetric profile with a peak in the center in **Fig. 6e**), and it is the deep-intermediate portion of the cortex which exhibits the strongest connectivity within the executive control network (peak towards the right in **Fig. 6e**). The shift in laminar connectivity preference towards the infragranular layers in the executive control network was evidenced, for instance, as stronger interhemispheric connections between intermediate layers of the middle frontal gyrus compared to its superficial layers (significant connections in yellow and orange but not blue, between some ROIs in **Fig. 6a**: "Executive control"). The laminar connectivity profile of each network computed for all subjects is presented in **Figure 6d**. From a global-ROI perspective, i.e., independent of cortical depth, our data presented multiple significant connections that were in agreement with the volume-based resting-state network results derived from an ICA analysis; volume-based examples and the corresponding depth-dependent profiles per ROI are shown in **Fig. S7**.

The identification of stronger connections involving the supragranular layers of the cortex in areas of the default mode network is in agreement with previous reports demonstrating a higher level of activity and communication near the surface of the cortex in humans and non-human primates during rest [69, 70].

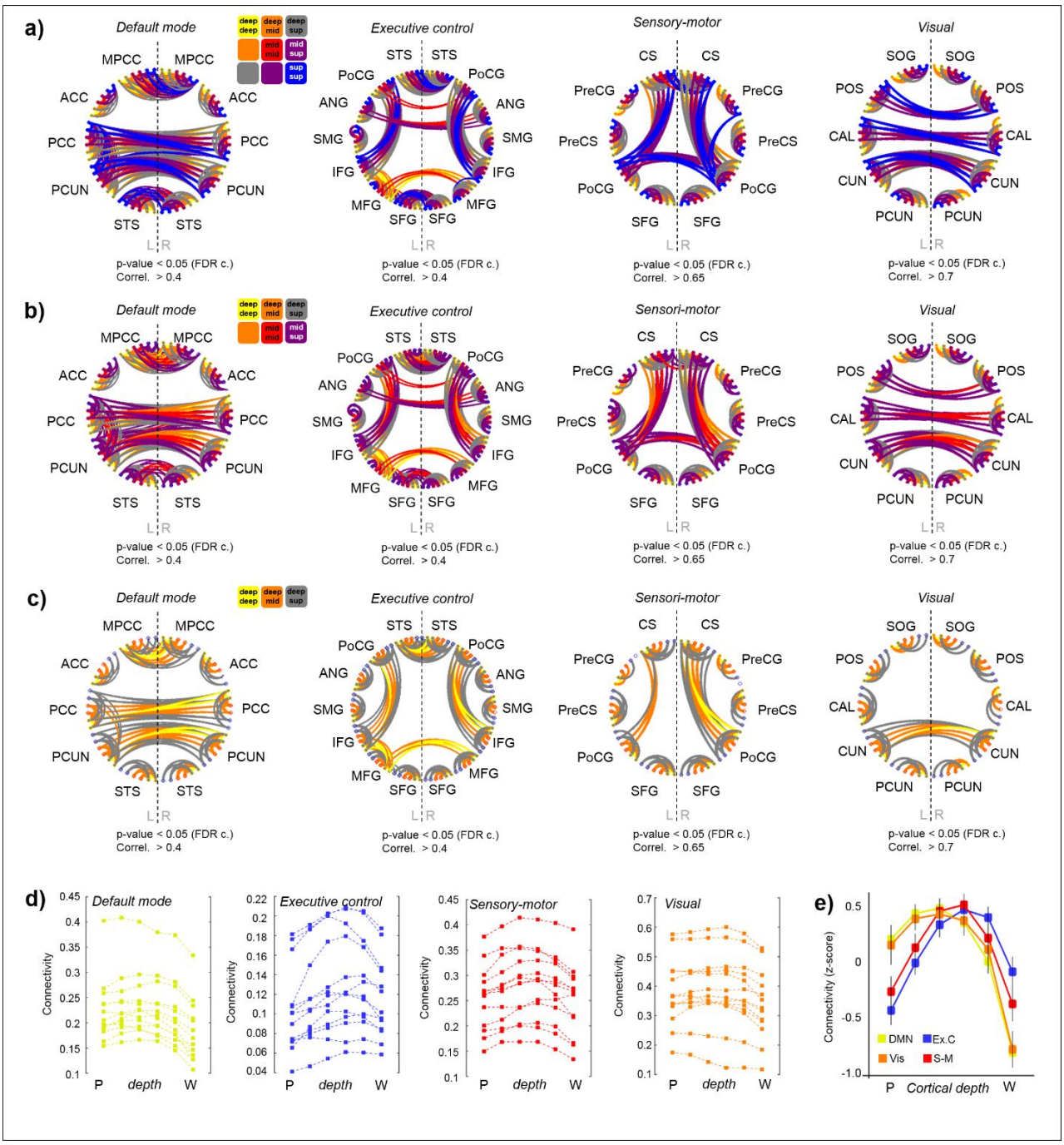


***Figure 6. Cortical depth-dependent functional connectivity. a)*** *Four graphs showing the layer-specific functional connections between ROIs engaged in four different brain networks. A legend is provided above the first graph. A version of these graphs hiding the top two superficial layers (i.e., only deep and intermediate layers are visible) and the two middle layers (i.e., only deep layers are visible) is provided in* ***b)*** *and* ***c)****, respectively.* ***d)*** *Each of the four graphs shows the averaged connectivity for each functional network at each cortical depth for all subjects included in the analysis.* ***e)*** *Cortical depth-specific global connectivity averaged in four resting-state networks. P: pial surface (near CSF); W: white matter. Error bars indicate ± standard error of the mean, N=13.*

### 3.5. State-dependent cortical-depth specificity of whole-brain functional measures

Having acquired whole-brain scans with high spatial specificity during rest and task performance, we aimed to assess the potential differences between both behavioral states at a laminar level. The slope or gradient of ALFF and ReHo measures along the cortical thickness, i.e., the difference between superficial and deep layers in terms of their signal amplitude and regional homogeneity, was significantly reduced when subjects were engaged in a motor task (**Fig. 7a** and 7**b**), suggesting that the superficial layers of the cortex are a major factor in the maintenance of resting-state activity that is significantly dampened during task performance.

Compared to task fMRI, resting-state scans generally exhibited higher connectivity between remote regions and their layers, as observed in their corresponding whole-brain connectivity graphs in **Fig. S4i-l** and in the network-specific graphs of **Fig. S5**. During the motor task, the connectivity within the executive control network seemed to involve more superficial layers of the cortex compared to rest (note the peak shift towards the left in the blue trace of **Fig. S4g or S4h** compared to **S4e**)). In contrast, more intermediate layers were involved in default mode network connectivity during task performance (yellow trace in **Fig. S4g or S4h** compared to **Fig. S4e,** and **Fig. 7c**). This was observed, for instance, as a stronger correlation between the anterior cingulate cortices of both cerebral hemispheres and a reduced interhemispheric connection of superior temporal and posterior mid-cingulate areas (**Fig. S5a**, middle graph, compared to the left graph).

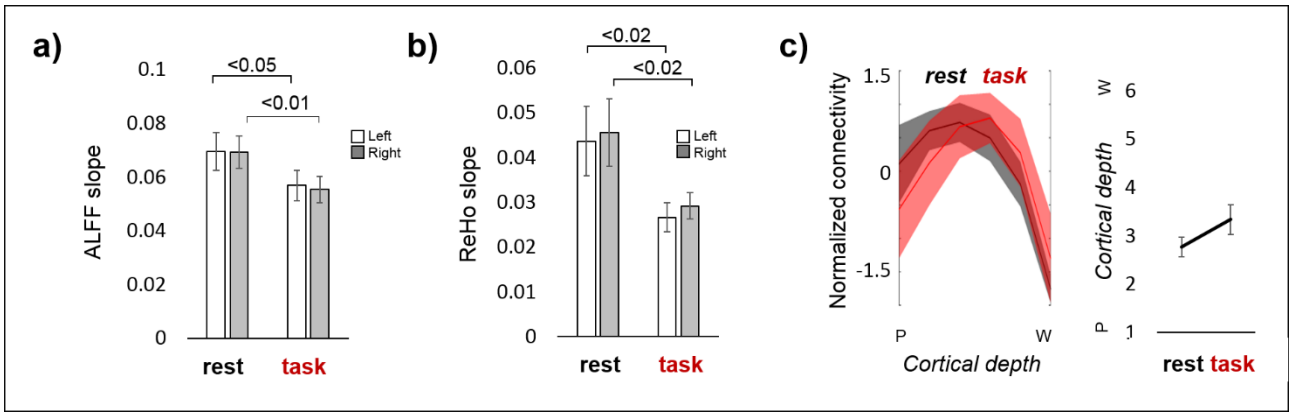


***Figure 7. Functional laminar differences between resting state and task. a)*** *The bar plot represents the average ALFF slope computed for the resting-state and the task scan (after regressing out the estimated task response).* ***b)*** *Average ReHo slope computed for the resting-state and the task scan (after regressing out the estimated task response). Values above the horizontal lines refer to the p-value of a t-test between conditions.* ***c)*** *Normalized mean ± standard error of the laminar connectivity profile in the default mode network during rest (black trace) and task (red trace), overlaid for comparison, and mean cortical depth at which the connectivity is maximum for each condition (not significantly different; the p-value of a t-test between conditions was 0.16). Error bars represent the standard error of the mean. N=13 for rs-fMRI-1 ("rest"); N=12 for task-fMRI ("task").*

## 4. DISCUSSION

The layer-specific communication patterns across distant brain regions of the human brain have remained largely unexplored, mainly due to the limited brain coverage afforded by most high-resolution methods. In this report, we employed a recently developed fMRI sequence (TR-external EPIK [58]) to address the question of how the different depths of the cerebral cortex participate in the maintenance of the resting state in humans. We first obtained motor-evoked responses that reproduced the laminar results seen in the existing literature and then provided a cortical-depth specific characterization of resting-state activity spanning multiple brain regions. Our ALFF showed a near-linear trend peaking at the surface of the cortex, likely reflecting vein-related bias, the slope of which was significantly reduced when subjects were engaged in a motor task. The slope of the mean ReHo across layers was also reduced during task performance, and network analysis showed certain differences both between networks and between conditions in terms of the cortical depth at which the connectivity was strongest, e.g., the DMN connectivity peaked at deeper layers in scans acquired during task performance. We interpreted the differences between resting-state and task as an indication that functional laminar dynamics can change with the brain state. Although our data may be partially contaminated by the influence of large veins (typical of GE sequences), certain metrics, especially those based on connectivity measures, demonstrated the sensitivity of the sequence to laminar events. Our results suggest that functional connections relevant to particular systems are cortical-depth specific, e.g. we found that intermediate and superficial cortical depths maintain key connectivity patterns in humans (e.g. DMN), in agreement with animal studies [10, 11], but we also identified a laminar connectivity shift towards deeper cortical layers in particular networks (e.g. EXEC).

In this study, we acquired two sets of rs-fMRI data for each subject within the same imaging session: one using isotropic voxels and the other using higher in-plane spatial resolution but with thicker slices. Both sets of data had voxels of similar volume (~ 0.25 $mm^3$). The resemblance between all functional measures assessed in both sets of the rs-fMRI data (**Fig. S4** and **S5**) suggests that both protocols were able to detect brain connectivity with layer-specificity to a similar level of performance. Given the agreement between both protocols, and since protocol-2 confers a more complete brain coverage, despite the non-isotropic voxel dimensions in protocol-2 ($0.51 \times 0.51 \times 1.00$ mm), it may be a better candidate than protocol-1 for whole-brain laminar fMRI, especially in applications where structures that are located at the base of the brain, e.g., hippocampus, brainstem, etc., are significant for the integrity of the study, as long as the high-resolution plane matches the right dimension in the target area. A more detailed technical description of both of the TR-external EPIK protocols can be found in reference [58].

In previous literature, higher activation of superficial, i.e., supragranular, cortical layers has been observed in laminar rs-fMRI studies that have focused on a restricted FOV in the human brain [69], in non-human primates [70], and in rodents [11]. In contrast to the granular layer, which receives thalamo-cortical afferents, and the deeper, i.e., infragranular, layers, which mainly initiate efferent responses through subcortical and spinal

projections, the superficial layers are the principal source and target of cortico-cortical regulatory communication [71-76]. Hereby, the deeper portion of layer III receives long distance feedforward projections, whereas its superficial portion, together with layer II, is targeted by long-distance feedback projections [40]. The present results support the supposition that superficial layers play a role in resting-state maintenance, as resting-state networks mostly involve cortical areas [42, 77]; however, our results also demonstrate a network-specific laminar connectivity profile, i.e., not all networks' connectivity peaked in intermediate/superficial territories. Although the literature upholds the results obtained from our resting-state analysis, i.e., strong participation of the superficial layers during rest, the GE nature of the sequence employed poses the question as to whether the recorded signal could be merely a reflection of a vascular-related superficial bias, potentially further enhanced by a higher SNR near the surface of the brain (i.e., stronger T2 signal near the CSF). While the amplitude of the fMRI signal was generally higher in the superficial layers (measured as ALFF during rest and also indicated by the larger evoked responses on the superficial layers during task performance), likely partially due to the higher signal produced in superficial vascular territories, the connectivity results shown here demonstrate that the ability of the fMRI sequence to map depth-specific connections was not compromised to the extent of masking interactions occurring below the surface of the cortex. In fact, the connectivity measures usually peaked in intermediate or more superficial layers but rarely on the most external layer of the cortex, and in some cases, the highest connectivity values were found in deeper territories. Besides, the fact that the layer-dependent signal amplitude, homogeneity, and whole-brain connectivity were significantly altered upon task performance using exactly the same imaging protocol (**Fig. 7**, **Fig. S4**, **Fig. S5**) suggests that a vein-related bias, if present, was not the only factor accounting for the observed responses. Notwithstanding this assertion, the potential implications of using a GE-based sequence will be discussed in a later paragraph.

In comparison to the resting-state paradigm, the assessment of layer-specific correlations during task performance revealed a decreased number of functional connections (**Fig. S4k** vs. **S4i**), which is in agreement with the literature [78]. The specificity of the responses evoked by the motor task was demonstrated with distinct line profiles in the precentral gyrus, in response to somatomotion, with and without somatosensation (**Fig. 3m**). Finger movement resulted in activation of the superficial and, to a lesser extent, deeper layers, the latter possibly indicating signaling from premotor and supplementary motor cortices, also coinciding with cortical motor efferents towards pontomedullary or thalamic nuclei [11, 79]. Sensory processing triggered by the touch between two fingers produced activation in intermediate layers, possibly reflecting the modulation of the motor cortex by sensory cortical areas and afferents from the sensory thalamus [11, 79, 80]. The activation observed near the cortical surface may reflect, at least to a certain extent, a contribution from the venous network; however, our laminar profiles do not merely represent a linear vein bias (**Fig. S3**). Moreover, superficial neuronal responses can be expected during the performance of a motor task, as motor thalamic afferents modulate motor behavior in superficial and intermediate layers of the cortex, in a similar way as the sensory thalamic afferents upon addition of touch [79], which has also been observed in laminar studies [18]. The fact that evoked responses in the intermediate and deep layers (**Fig. 3j**) were detected in a line-profile

analysis but not in the analysis of a bigger cortical patch, also responding to the motor task but exhibiting an upper → deeper trend only, demonstrates the specificity of the laminar responses on particular cortical regions and the overall preponderance of BOLD responses in the superficial layers in less specific evaluations. Although some corrections could be applied to the evoked responses to compensate for the vasculature-related gradient, we deferred from using this procedure. This was done to avoid masking the contribution of non-neuronal sources that would be present in the resting state data, i.e., we opted for applying the same correction to task and resting-state data, as correction of the latter using existing models is currently not straightforward.

It could be argued that, aside from the potential venous influence, the higher SNR in the superficial layers (e.g., Fig. 3f, upper layers showing higher mean MR signal in the TR-external EPIK image) could facilitate the detection of functional responses and connections between superficial cortical depths. However, as superficial, intermediate, and deep connections pertaining to different network systems were detected differently during task performance and during rest (e.g., **Fig. 7c**, **Fig. S4**, **Fig. S5**), and the ALFF and ReHo gradients were reduced during task performance (**Fig. 7a-b**), it is likely that functional information remains in the high-resolution data despite potential bias in favor of the superficial layers; i.e., not all activations and connections were observed in the most external layer of the cortex or to the same extent, independent of the behavioral condition. The evaluation of typical resting-state measures in our task-fMRI scans after regression of model activation responses provided a reference framework of potential changes at the level of cortical laminae relevant to the brain state. Although most connections that are typically found during resting-state exist in task-related data, our results showed that the preferred layers to maintain such connections can change, e.g., the DMN during task appears less supported by superficial layers than during rest (**Fig. 7c**, **Fig. S4g vs. S4e** and **Fig. 5a**).

The selected fMRI sequence integrates a number of acceleration techniques that enable a large matrix with fine resolution to be sampled without compromising the quality of the data (the sequence implementation has been previously demonstrated in comparison to EPI [53, 54]). In TR-external EPIK, the high spatial resolution is partially possible due to the segmented sampling of the k-space periphery. While full k-space sampling is completed every 3 TRs, the combination of this with a fully sampled center k-space at each TR confers upon TR-external EPIK enough temporal resolution to sample brain hemodynamics with sub-millimetre resolution ([53, 54, 57, 58, 81]). The results from the group of subjects studied in this work demonstrate the feasibility of using TR-external EPIK for the detection of layer-specific functional signals. In our protocol, the sharing of missing k-space lines is limited to the adjacent two scans, the energy of which was determined to be smaller than 10% of the entire k-space energy. Although the peripheral k-space is updated slowly (i.e. 3 TRs = 10.5 s; ~0.1 Hz), it is sufficient to track the change of resting-state signals, the peaks of which are usually detected within a frequency of 0.03-0.04 Hz [64-67] in the gray matter. Furthermore, it has been reported that conventional resting-state analyses are not significantly altered by TR [82], and methods employing relatively slow sampling have succeeded in tracking laminar dynamics (e.g. 3960ms [45], 5000ms [83], 8300ms [84]). Despite the advantages of TR-external EPIK over conventional EPI, the GE nature of the technique, makes it

susceptible to vein-derived contamination, just as any other GE-EPI sequence. Assuming a fair neuro-vascular coupling, the fMRI signal extracted from a cortical capillary network is a reliable indicator of neuronal activity. However, capillaries supplying blood to neurons flow in bigger ascending venules that run perpendicular to the cortex and disgorge into pial veins tangential to the surface of the brain, and these veins influence the fMRI signal and can result in a bias towards the superficial layers of the cortex. This bias is reduced in other acquisition schemes, such as SE-BOLD fMRI, sensitive to oxygenation changes in the microvasculature only, vascular space occupancy fMRI (VASO), sensitive to vessel dilation, or cerebral blood flow-based fMRI (CBF), sensitive to flow changes. Due to the short T2 constant of blood at ultra-high field, BOLD-fMRI at 7T is only sensitive to the extra-vascular effect of the oxy/deoxy-hemoglobin ratio, irrespective of vessels size. Although the parenchymal vessels, i.e., venules of diameter < 25 μm, are detected by both SE- and GE-BOLD, these are often overshadowed in GE sequences by the influence of bigger veins running along the surface of the brain, which cause static perturbations in the magnetic field affecting the neighboring parenchymal tissue. Therefore, while SE-BOLD offers a fine localization of the activated parenchyma, GE-BOLD provides a mixed signal that is relevant to both small parenchymal vessels and macroscopic veins. To correct for this bias, we subtracted the time-varying phase component of the MR signal from each voxel's magnitude time course. The time-varying phase component is proportional to the frequency offset exhibited by the spins and hence, sensitive to the venous vasculature [30, 31]. As large vessels produce field inhomogeneities, spins processing in the neighboring parenchyma would produce changes in the phase component of the signal; in contrast, small randomly oriented vessels, e.g., in the capillary network within the gray matter, do not produce a net phase and hence, their derived signal remains intact. Although this method helps to improve the local specificity of BOLD, several biases could remain in the corrected data, such as those derived from motion correction or geometric distortions [85], which reduce the ultimate spatial resolution of GE sequences. However, it is worth noting that geometric distortions are less pronounced in EPIK compared to conventional EPI, and in fact, the PSF of GE-EPIK is narrower than in conventional GE-EPI [53]. Additionally, the frequency offsets derived from field inhomogeneities around vessels that are oriented parallel to the B0 field cannot be compensated for during the post-processing [86]. A few groups have demonstrated the dependence of laminar fMRI on the orientation of the cortex with respect to B0 [86, 87]. Although orientation bias can be critical for the dissection of the fMRI signal, this effect has been correlated with low-frequency drift, motion, and respiratory cycles, which were accounted for in our study, therefore diminishing the discussed effect. Moreover, most of our results were obtained from relatively big patches of the cortex and through multiple ROIs, averaging vertices with different orientations within a cortical surface. Hence, although non-negligible, an orientation bias is not expected to have conditioned our results. However, a future model accounting for such an effect could determine the extent to which the curvature affects the laminar profiles at a whole-brain level.

In contrast to retrospective model-based approaches that reduce the superficial BOLD bias by applying temporal decomposition [36], linear detrending [32], normalization [33], or deconvolution [34, 35] to evoked fMRI data, the phase-based correction method employed here does not involve a priori assumptions about the behavior of the vascular dynamics across the cortical thickness and does not rely on the use of an evoked

paradigm, offering a bias-free alternative to correct resting-state GE-fMRI data. Based on our results, this phase-based method [30] may constitute a rather conservative approach, i.e., the activity of the superficial layers was found to predominate almost ubiquitously (higher ALFF in upper layers of the cortex). However, connectivity analysis did identify laminar interactions in a cortical profile different from the linear gradient that would be expected in purely macro-vascular measures, i.e., with a maximum on the surface, and the evoked responses were composed of two peaks, the latter located in deeper layers of the cortex, indicating a decent laminar sensitivity. Future studies employing GE TR-external EPIK and SE TR-external EPIK, in a combined acquisition, will investigate the possibility of complementing the phase-correction method with additional strategies to exploit the high SNR of GE schemes with robust laminar specificity.

The vascular dependence of the fMRI signal remains one of the biggest challenges in laminar fMRI [88]. Signals obtained with BOLD contrast are not only conditioned by a physically-constrained laminar point-spread function, i.e., the fact that ascending venules spread the deep activation signals towards superficial layers [35, 89, 90], but also by the varying physiological mechanisms underlying the BOLD response (CBF, CMRO2, CBV), which can modulate this point-spread function across cortical layers [89]. Despite the complexity of the model, laminar fMRI studies have even employed strategies that artificially sample the cortical depth with a number of points higher than the number of voxels across the cortical ribbon. This is appropriate under the assumption that the purpose of the study is tracking the trend of activation across the cortical depth and not to resolve the actual neuronal signal at any particular layer, which is indeed not possible, even with sufficient spatial resolution, given the facts discussed above. In this study, the number of depths used was equal to the number of histologically-defined layers in the neocortex; however, the layers in our model have been arbitrarily chosen to be equally spaced along the cortical thickness and have no direct relationship with the cortical cytoarchitecture. Hence, our conclusions should be interpreted in terms of cortical depth only. Although some reports have chosen a smaller number of layers for their laminar assessment, e.g., three [45], which simplifies the analysis and confers layers with a greater independence, others have shown that a greater number of depths, e.g., twenty [18], enables clearer detection of cortical responses, despite the fact that this strategy involves a greater dependence on neighbor signals. In addition, the latter scheme also poses an important challenge in whole-brain studies due to the high computational demands of the analysis procedure (see discussion below).

Irrespective of the number of layers, ambitious whole-brain laminar fMRI studies should assure perfect co-registration between the anatomical reference scan and the functional data. Previous reports have shown the possibility of integrating T1 contrast within a high-resolution fMRI sequence (e.g., [18], acquired during VASO), which allows a 1:1 relationship between the anatomical and functional scans, mitigating any co-registration concern. This option was not yet available in the current study. Nevertheless, in this work, we achieved acceptable co-registration in the majority of the brain by using manual rigid transformations (**Fig. S8**), which proved to be more reliable than the transformations rendered by non-linear automatic registration tools. In addition, the improved robustness against geometric distortions in TR-external EPIK [53] is expected

to yield fewer co-registration errors, compared to the common EPI, between the functional scans and the anatomical scans (e.g., MR2RAGE). However, particular areas in different subjects remained poorly co-registered and needed to be masked out to ensure a proper laminar analysis. In the future, TR-external EPIK will be modified to provide a T1 contrast, which will avoid data loss, reduce the pre-processing time, and, more importantly, will alleviate the potential concerns relating to co-registration.

In this work, we employed TR-external EPIK to map the majority of the brain with a voxel resolution of 0.63 × 0.63 × 0.63 $mm^3$ or 0.51 × 0.51 × 1.00 $mm^3$. In addition to the challenge in terms of sequence design, the resulting matrix size imaged by TR-external EPIK (336 × 336 × 123 or 408 × 408 × 108) presents important computational limitations in post-processing, such as the relatively large memory required (minimum storage space: ~ 6 Gb per 4D-volume; RAM: ≥ 32Gb for many pre-processing steps) and long processing times. After pre-processing, analysis of the cortical surfaces with numerical computing environments such as Matlab is, again, conditioned by the number of vertices to be processed. Therefore, the greater the number of layers, the higher the computational demands. For instance, one cortical surface covered by protocol-1 contained ~ 290,000 vertices, which means that the six surfaces obtained from both hemispheres involved the analysis of ~ 3,480,000 vertices, each of them consisting of a 168-point time course. In this work, in order to adjust the computational demands to those of a standard scientific workstation, the first step in most of the layer-specific functional analyses was to average all vertices specific to one layer within one ROI. Given that the laminar performance of the cortex can be highly localized, some events might be overlooked when using an ROI-based analysis to identify particular behaviors; hence, the use of supercomputing resources to assess vertex-specific measures becomes highly desirable to exploit the information contained in the acquired data.

## 5. CONCLUSIONS

This study adopted a sequence offering high spatial resolution (~ 0.25 $mm^3$ voxels) to map laminar functional dynamics in a 7T scanner with near whole-brain mapping in healthy subjects. We investigated the dependence of common rs-fMRI measures such as ALFF, ReHo, and functional connectivity on cortical depth, which has emerged as a new dimension to be explored in the human brain. Our results indicate that the cortical depth is differentially (functionally) connected depending on the resting-state network, with intermediate and superficial layers playing a critical role in the maintenance of the DMN, and further show that the laminar involvement can change during a motor task. This work demonstrates the potential of laminar analysis of connectivity in the study of broad cortical networks.

**References:**


1. Palomero-Gallagher, N. and K. Zilles, *Cortical layers: Cyto-, myelo-, receptor- and synaptic architecture in human cortical areas.* Neuroimage, 2019. **197**: p. 716-741.
2. Thomson, A.M. and A.P. Bannister, *Interlaminar connections in the neocortex.* Cereb Cortex, 2003. **13**(1): p. 5-14.
3. Larkum, M.E., et al., *A Perspective on Cortical Layering and Layer-Spanning Neuronal Elements.* Front Neuroanat, 2018. **12**: p. 56.
4. Michelson, N.J. and T.D.Y. Kozai, *Isoflurane and ketamine differentially influence spontaneous and evoked laminar electrophysiology in mouse V1.* J Neurophysiol, 2018. **120**(5): p. 2232-2245.
5. Krupa, D.J., et al., *Layer-specific somatosensory cortical activation during active tactile discrimination.* Science, 2004. **304**(5679): p. 1989-92.
6. Adesnik, H. and A. Naka, *Cracking the Function of Layers in the Sensory Cortex.* Neuron, 2018. **100**(5): p. 1028-1043.
7. Ayaz, A., et al., *Layer-specific integration of locomotion and sensory information in mouse barrel cortex.* Nat Commun, 2019. **10**(1): p. 2585.
8. Scott, B.B., et al., *Imaging Cortical Dynamics in GCaMP Transgenic Rats with a Head-Mounted Widefield Macroscope.* Neuron, 2018. **100**(5): p. 1045-1058 e5.
9. Csercsa, R., et al., *Laminar analysis of slow wave activity in humans.* Brain, 2010. **133**(9): p. 2814-29.
10. Whitesell, J.D., et al., *Regional, Layer, and Cell-Type-Specific Connectivity of the Mouse Default Mode Network.* Neuron, 2021. **109**(3): p. 545-559 e8.
11. Weiler, N., et al., *Top-down laminar organization of the excitatory network in motor cortex.* Nat Neurosci, 2008. **11**(3): p. 360-6.
12. Logothetis, N.K., et al., *Neurophysiological investigation of the basis of the fMRI signal.* Nature, 2001. **412**(6843): p. 150-7.
13. Logothetis, N.K., *The neural basis of the blood-oxygen-level-dependent functional magnetic resonance imaging signal.* Philos Trans R Soc Lond B Biol Sci, 2002. **357**(1424): p. 1003-37.
14. Ogawa, S., et al., *Brain magnetic resonance imaging with contrast dependent on blood oxygenation.* Proc Natl Acad Sci U S A, 1990. **87**(24): p. 9868-72.
15. Yu, X., et al., *Deciphering laminar-specific neural inputs with line-scanning fMRI.* Nat Methods, 2014. **11**(1): p. 55-8.
16. Lawrence, S.J.D., et al., *Laminar fMRI: Applications for cognitive neuroscience.* Neuroimage, 2019. **197**: p. 785-791.
17. Guidi, M., et al., *Lamina-dependent calibrated BOLD response in human primary motor cortex.* Neuroimage, 2016. **141**: p. 250-261.
18. Huber, L., et al., *High-Resolution CBV-fMRI Allows Mapping of Laminar Activity and Connectivity of Cortical Input and Output in Human M1.* Neuron, 2017. **96**(6): p. 1253-1263 e7.
19. Chai, Y., et al., *Integrated VASO and perfusion contrast: A new tool for laminar functional MRI.* Neuroimage, 2020. **207**: p. 116358.
20. Huber, L., et al., *Cortical lamina-dependent blood volume changes in human brain at 7 T.* Neuroimage, 2015. **107**: p. 23-33.
21. Ress, D., et al., *Laminar profiles of functional activity in the human brain.* Neuroimage, 2007. **34**(1): p. 74-84.
22. Polimeni, J.R., et al., *Laminar analysis of 7T BOLD using an imposed spatial activation pattern in human V1.* Neuroimage, 2010. **52**(4): p. 1334-46.
23. Kashyap, S., et al., *Resolving laminar activation in human V1 using ultra-high spatial resolution fMRI at 7T.* Sci Rep, 2018. **8**(1): p. 17063.

24. van Mourik, T., et al., *Laminar signal extraction over extended cortical areas by means of a spatial GLM.* PLoS One, 2019. **14**(3): p. e0212493.
25. De Martino, F., et al., *Frequency preference and attention effects across cortical depths in the human primary auditory cortex.* Proc Natl Acad Sci U S A, 2015. **112**(52): p. 16036-41.
26. Lu, H., et al., *Functional magnetic resonance imaging based on changes in vascular space occupancy.* Magn Reson Med, 2003. **50**(2): p. 263-74.
27. Huber, L., et al., *Ultra-high resolution blood volume fMRI and BOLD fMRI in humans at 9.4T: Capabilities and challenges.* Neuroimage, 2018. **178**: p. 769-779.
28. Poplawsky, A.J., et al., *Layer-Specific fMRI Responses to Excitatory and Inhibitory Neuronal Activities in the Olfactory Bulb.* J Neurosci, 2015. **35**(46): p. 15263-75.
29. Kay, K., et al., *A critical assessment of data quality and venous effects in sub-millimeter fMRI.* Neuroimage, 2019. **189**: p. 847-869.
30. Menon, R.S., *Postacquisition suppression of large-vessel BOLD signals in high-resolution fMRI.* Magn Reson Med, 2002. **47**(1): p. 1-9.
31. Curtis, A.T., R.M. Hutchison, and R.S. Menon, *Phase based venous suppression in resting-state BOLD GE-fMRI.* Neuroimage, 2014. **100**: p. 51-9.
32. Fracasso, A., et al., *Laminar imaging of positive and negative BOLD in human visual cortex at 7T.* Neuroimage, 2018. **164**: p. 100-111.
33. Kashyap, S., et al., *Impact of acquisition and analysis strategies on cortical depth-dependent fMRI.* Neuroimage, 2018. **168**: p. 332-344.
34. Heinzle, J., et al., *A hemodynamic model for layered BOLD signals.* Neuroimage, 2016. **125**: p. 556-570.
35. Markuerkiaga, I., M. Barth, and D.G. Norris, *A cortical vascular model for examining the specificity of the laminar BOLD signal.* Neuroimage, 2016. **132**: p. 491-498.
36. Kay, K., et al., *A temporal decomposition method for identifying venous effects in task-based fMRI.* Nat Methods, 2020. **17**(10): p. 1033-1039.
37. Siero, J.C., et al., *Cortical depth-dependent temporal dynamics of the BOLD response in the human brain.* J Cereb Blood Flow Metab, 2011. **31**(10): p. 1999-2008.
38. Muckli, L., et al., *Contextual Feedback to Superficial Layers of V1.* Curr Biol, 2015. **25**(20): p. 2690-5.
39. Yacoub, E., N. Harel, and K. Ugurbil, *High-field fMRI unveils orientation columns in humans.* Proc Natl Acad Sci U S A, 2008. **105**(30): p. 10607-12.
40. Zilles, K. and M. Catani, *Cerebral hemispheres*, in *Gray's Anatomy*. 2020.
41. Scheeringa, R., et al., *The relationship between oscillatory EEG activity and the laminar-specific BOLD signal.* Proc Natl Acad Sci U S A, 2016. **113**(24): p. 6761-6.
42. Raichle, M.E., et al., *A default mode of brain function.* Proc Natl Acad Sci U S A, 2001. **98**(2): p. 676-82.
43. Polimeni, J., Witzel,T.,and Fischl, B. , *Identifying common-source driven correlations in resting-state fMRI via laminar-specific analysis in the human visual cortex.* Proc Intl Soc Mag Reson Med, 2010. **18**: p. 353.
44. De Martino, F., et al., *Whole brain high-resolution functional imaging at ultra high magnetic fields: an application to the analysis of resting state networks.* Neuroimage, 2011. **57**(3): p. 1031-44.
45. Sharoh, D., et al., *Laminar specific fMRI reveals directed interactions in distributed networks during language processing.* Proc Natl Acad Sci U S A, 2019. **116**(42): p. 21185-21190.
46. Huber, L., et al., *Layer-dependent functional connectivity methods.* Prog Neurobiol, 2020: p. 101835.
47. Shah, N.J., Zilles, K., *Verfahren zur Untersuchung eines Objektes mittels Erfassung des Ortsfrequenzraumes*. 2003.
48. Shah NJ, a.Z.K., *Imaging process in the spatial frequency space and useful for examining the properties of object*. 2004.

49. Zaitsev, M., K. Zilles, and N.J. Shah, *Shared k-space echo planar imaging with keyhole.* Magn Reson Med, 2001. **45**(1): p. 109-17.
50. Zaitsev, M., et al., *Dual-contrast echo planar imaging with keyhole: application to dynamic contrast-enhanced perfusion studies.* Phys Med Biol, 2005. **50**(19): p. 4491-505.
51. Yun, S., Pais-Roldan, P., Shah, NJ., *Detection of Cortical Depth-dependent Functional Activation using Whole-brain, Half-millimetre Resolution EPIK at 7T.* ISMRM, Sydney, Australia, 2020.
52. Yun, S.D. and N.J. Shah, *Analysis of EPI phase correction with low flip-angle excitation to reduce the required minimum TE: Application to whole-brain, submillimeter-resolution fMRI at 3 T.* Magn Reson Med, 2020. **84**(3): p. 1416-1429.
53. Yun, S.D., et al., *Parallel imaging acceleration of EPIK for reduced image distortions in fMRI.* Neuroimage, 2013. **73**: p. 135-43.
54. Yun, S.D. and N.J. Shah, *Whole-brain high in-plane resolution fMRI using accelerated EPIK for enhanced characterisation of functional areas at 3T.* PLoS One, 2017. **12**(9): p. e0184759.
55. Caldeira, L.L., et al., *Dynamic susceptibility contrast parametric imaging using accelerated dual-contrast echo planar imaging with keyhole.* J Magn Reson Imaging, 2019. **50**(2): p. 628-640.
56. Shah, N.J., N.A. da Silva, and S.D. Yun, *Perfusion weighted imaging using combined gradient/spin echo EPIK: Brain tumour applications in hybrid MR-PET.* Hum Brain Mapp, 2019.
57. Yun, S.D., et al., *Evaluating the Utility of EPIK in a Finger Tapping fMRI Experiment using BOLD Detection and Effective Connectivity.* Sci Rep, 2019. **9**(1): p. 10978.
58. Yun, S., Pais-Roldán, P., Palomero-Gallagher, N., Shah, N. J., *Mapping of Whole-Brain Resting-State Networks with HalfMillimetre Resolution.* Human Brain Mapping, 2022.
59. Schweisfurth, M.A., et al., *Comparison of fMRI Digit Representations of the Dominant and Non-dominant Hand in the Human Primary Somatosensory Cortex.* Front Hum Neurosci, 2018. **12**: p. 492.
60. Glover, G.H., T.Q. Li, and D. Ress, *Image-based method for retrospective correction of physiological motion effects in fMRI: RETROICOR.* Magn Reson Med, 2000. **44**(1): p. 162-7.
61. Stanley, O.W., et al., *Effects of phase regression on high-resolution functional MRI of the primary visual cortex.* Neuroimage, 2021. **227**: p. 117631.
62. Xu, T., Yang, Z., Jiang, L., Xing, X., Zuo, X., *A Connectome Computation System for discovery science of brain.* Science Bulletin, 2015. **60**(1): p. 89-95.
63. Geyer, S., et al., *Two different areas within the primary motor cortex of man.* Nature, 1996. **382**(6594): p. 805-7.
64. Zuo, X.N., et al., *The oscillating brain: complex and reliable.* Neuroimage, 2010. **49**(2): p. 1432-45.
65. Xue, S.W., et al., *Different neural manifestations of two slow frequency bands in resting functional magnetic resonance imaging: a systemic survey at regional, interregional, and network levels.* Brain Connect, 2014. **4**(4): p. 242-55.
66. Yuen, N.H., N. Osachoff, and J.J. Chen, *Intrinsic Frequencies of the Resting-State fMRI Signal: The Frequency Dependence of Functional Connectivity and the Effect of Mode Mixing.* Front Neurosci, 2019. **13**: p. 900.
67. Bajaj, S., et al., *Oscillatory motor network activity during rest and movement: an fNIRS study.* Front Syst Neurosci, 2014. **8**: p. 13.
68. Murphy, K., R.M. Birn, and P.A. Bandettini, *Resting-state fMRI confounds and cleanup.* Neuroimage, 2013. **80**: p. 349-59.
69. Guidi, M., et al., *Cortical laminar resting-state signal fluctuations scale with the hypercapnic blood oxygenation level-dependent response.* Hum Brain Mapp, 2020. **41**(8): p. 2014-2027.
70. Mishra, A., et al., *Functional connectivity with cortical depth assessed by resting state fMRI of subregions of S1 in squirrel monkeys.* Hum Brain Mapp, 2019. **40**(1): p. 329-339.

71. Moerel, M., et al., *Processing complexity increases in superficial layers of human primary auditory cortex.* Sci Rep, 2019. **9**(1): p. 5502.
72. D'Souza, R.D. and A. Burkhalter, *A Laminar Organization for Selective Cortico-Cortical Communication.* Front Neuroanat, 2017. **11**: p. 71.
73. Rubio-Garrido, P., et al., *Thalamic input to distal apical dendrites in neocortical layer 1 is massive and highly convergent.* Cereb Cortex, 2009. **19**(10): p. 2380-95.
74. Larkum, M.E., *The yin and yang of cortical layer 1.* Nat Neurosci, 2013. **16**(2): p. 114-5.
75. Sempere-Ferrandez, A., S. Martinez, and E. Geijo-Barrientos, *Synaptic mechanisms underlying the intense firing of neocortical layer 5B pyramidal neurons in response to cortico-cortical inputs.* Brain Struct Funct, 2019. **224**(4): p. 1403-1416.
76. Rolls, E.T. and W.P.C. Mills, *Computations in the deep vs superficial layers of the cerebral cortex.* Neurobiol Learn Mem, 2017. **145**: p. 205-221.
77. Heine, L., et al., *Resting state networks and consciousness: alterations of multiple resting state network connectivity in physiological, pharmacological, and pathological consciousness States.* Front Psychol, 2012. **3**: p. 295.
78. Jurkiewicz, M.T., A.P. Crawley, and D.J. Mikulis, *Is Rest Really Rest? Resting-State Functional Connectivity During Rest and Motor Task Paradigms.* Brain Connect, 2018. **8**(5): p. 268-275.
79. Hooks, B.M., et al., *Organization of cortical and thalamic input to pyramidal neurons in mouse motor cortex.* J Neurosci, 2013. **33**(2): p. 748-60.
80. Mao, T., et al., *Long-range neuronal circuits underlying the interaction between sensory and motor cortex.* Neuron, 2011. **72**(1): p. 111-23.
81. Yun, S. and N.J. Shah, *Full-FOV, Whole-brain, Half-millimetre Resolution fMRI at 7T using Accelerated multi-band EPIK with TR-external Phase Correction*, in *27th Annual Meeting of ISMRM*. 2019: Montreal, Canada.
82. Huotari, N., et al., *Sampling Rate Effects on Resting State fMRI Metrics.* Front Neurosci, 2019. **13**: p. 279.
83. Barry, R.L., et al., *Ultra-high field (7T) functional magnetic resonance imaging in amyotrophic lateral sclerosis: a pilot study.* Neuroimage Clin, 2021. **30**: p. 102648.
84. Huber, L., et al., *Layer-dependent functional connectivity methods.* Prog Neurobiol, 2021. **207**: p. 101835.
85. Bause, J., et al., *Impact of prospective motion correction, distortion correction methods and large vein bias on the spatial accuracy of cortical laminar fMRI at 9.4 Tesla.* Neuroimage, 2019. **208**: p. 116434.
86. Viessmann, O., et al., *Dependence of resting-state fMRI fluctuation amplitudes on cerebral cortical orientation relative to the direction of B0 and anatomical axes.* Neuroimage, 2019. **196**: p. 337-350.
87. Baez-Yanez, M.G., et al., *The impact of vessel size, orientation and intravascular contribution on the neurovascular fingerprint of BOLD bSSFP fMRI.* Neuroimage, 2017. **163**: p. 13-23.
88. Uludag, K. and P. Blinder, *Linking brain vascular physiology to hemodynamic response in ultra-high field MRI.* Neuroimage, 2018. **168**: p. 279-295.
89. Havlicek, M. and K. Uludag, *A dynamical model of the laminar BOLD response.* Neuroimage, 2020. **204**: p. 116209.
90. Marquardt, I., et al., *Cortical depth profiles of luminance contrast responses in human V1 and V2 using 7 T fMRI.* Hum Brain Mapp, 2018. **39**(7): p. 2812-2827.

**Tables:**

**Table 1. Regions of interest.**

| Abb. ROI | Full ROI name | Related network(s) |
|---|---|---|
| MPCC | Posterior Midcingulate Cortex | DMN |
| ACC | Anterior Cingulate Cortex | DMN |
| PCC | Posterior Cingulate Cortex | DMN |
| PCUN | Precuneus | DMN & VISUAL |
| STS | Superior Temporal Sulcus | DMN & EXEC |
| PoCG | Postcentral Gyrus | EXEC & SM |
| ANG | Inferior Parietal - angular | EXEC |
| SMG | Inferior Parietal - supramarginal | EXEC |
| IFG | Inferior Frontal G&S | EXEC |
| MFG | Middle Frontal Gyrus | EXEC |
| SFG | Superior Frontal G&S | EXEC & SM |
| SOG | Superior Occipital Gyrus | VISUAL |
| POS | Parieto-occipital Sulcus | VISUAL |
| CAL | Calcarine | VISUAL |
| CUN | Cuneus | VISUAL |
| CS | Central Sulcus | SM |
| PreCG | Precentral Gyrus | SM |
| PreCS | Precentral Sulcus | SM |
| STG | Superior Temporal Gyrus | AUDITORY |
| SubCG | Subcentral G&S | AUDITORY |
| MACG | Anterior Midcingulate Cortex | SALIENCE |

**Table 1.** DMN: default mode network; EXEC: executive control network; SM: sensory-motor network. ROIs extracted from the Freesurfer surface parcellation *aparc.a2009s.annot*, based on the Destrieux atlas.